Atomic scattering factor of the ASTRO-H (Hitomi) SXT reflector around the gold's L edges

Kikuchi, Naomichi; Kurashima, Sho; Ishida, Manabu; Iizuka, Ryo; Maeda, Yoshitomo; Hayashi, Takayuki; Okajima, Takashi; Matsumoto, Hironori; Mitsuishi, Ikuyuki; Saji, Shigetaka

Total number of authors:
17

Published in:
Optics Express

Link to article, DOI:
10.1364/OE.24.025548

Publication date:
2016

Document Version
Publisher's PDF, also known as Version of record

Research Article | Vol. 24, No. 22 | 31 Oct 2016 | OPTICS EXPRESS 25548
Optics EXPRESS

Atomic scattering factor of the ASTRO-H (Hitomi) SXT reflector around the gold's L edges

NAOMICHI KIKUCHI,[1,2] SHO KURASHIMA,[1,2] MANABU ISHIDA,[1,2,3] RYO IIZUKA,[1] YOSHITOMO MAEDA,[1,3,*] TAKAYUKI HAYASHI,[4,5] TAKASHI OKAJIMA,[5] HIRONORI MATSUMOTO,[4] IKUYUKI MITSUISHI,[4] SHIGETAKA SAJI,[4] TOSHIKI SATO,[1,2] SASAGU TACHIBANA,[4] HIDEYUKI MORI,[5] FINN CHRISTENSEN,[6] NICOLAI BREJNHOLT,[7] KIYOFUMI NITTA,[8] AND TOMOYA URUGA[8]

[1]*Tokyo Metropolitan University, 1-1 Minami-Osawa, Hachioji, Tokyo 192-0397, Japan*
[2]*Institute of Space and Astronautical Science (ISAS), Japan Aerospace Exploration Agency (JAXA), 3-1-1 Yoshinodai, Sagamihara, 229-8510, Japan*
[3]*The Graduate University for Advanced Studies, 3-1-1 Yoshinodai, Chuo-ku, Sagamihara, Kanagawa 252-5210, Japan*
[4]*Nagoya University, Furo-cho, Chikusa-ku, Nagoya 464-8602, Japan*
[5]*NASA Goddard Space Flight Center, Code 662, Greenbelt, MD 20771, USA*
[6]*DTU Space, National Space Institute, Technical University of Denmark, Elektrovej 327, DK-2800 Lyngby, Denmark*
[7]*Lawrence Livermore National Laboratory, Livermore, CA 94550, USA*
[8]*JASRI/SPring-8, Sayo-cho, Sayo, Hyogo 679-5198, Japan*
[*]*ymaeda@astro.isas.jaxa.jp*

Abstract: The atomic scattering factor in the energy range of 11.2–15.4 keV for the ASTRO-H Soft X-ray Telescope (SXT) is reported. The large effective area of the SXT makes use of photon spectra above 10 keV viable, unlike most other X-ray satellites with total-reflection mirror optics. Presence of gold's L-edges in the energy band is a major issue, as it complicates the function of the effective area. In order to model the area, the reflectivity measurements in the 11.2–15.4 keV band with the energy pitch of 0.4 – 0.7 eV were made in the synchrotron beamline Spring-8 BL01B1. We obtained atomic scattering factors f1 and f2 by the curve fitting to the reflectivities of our witness sample. The edges associated with the L-I, II, and III transitions are identified, of which the depths are found to be roughly 60% shallower than those expected from the Henke's atomic scattering factor.

OCIS codes: (340.7470) X-ray mirrors; (300.6560) Spectroscopy, X-ray.

References and links

1. T. Takahashi, K. Mitsuda, R. Kelley, F. Aharonian, H. Akamatsu, F. Akimoto, S. Allen, N. Anabuki, L. Angelini, K. Arnaud, M. Asai, M. Audard, H. Awaki, P. Azzarello, C. Baluta, A. Bamba, N. Bando, M. Bautz, T. Bialas, R. D. Blandford, K. Boyce, L. Brenneman, G. Brown, E. Cackett, E. Canavan, M. Chernyakova, M. Chiao, P. Coppi, E. Costantini, J. de Plaa, J.-W. den Herder, M. DiPirro, C. Done, T. Dotani, J. Doty, K. Ebisawa, T. Enoto, Y. Ezoe, A. Fabian, C. Ferrigno, A. Foster, R. Fujimoto, Y. Fukazawa, S. Funk, A. Furuzawa, M. Galeazzi, L. Gallo, P. Gandhi, K. Gilmore, M. Guainazzi, D. Haas, Y. Haba, K. Hamaguchi, A. Harayama, I. Hatsukade, K. Hayashi, T. Hayashi, K. Hayashida, J. Hiraga, K. Hirose, A. Hornschemeier, A. Hoshino, J. Hughes, U. Hwang, R. Iizuka, Y. Inoue, K. Ishibashi, M. Ishida, K. Ishikawa, K. Ishimura, Y. Ishisaki, M. Itoh, N. Iwata, N. Iyomoto, C. Jewell, J. Kaastra, T. Kallman, T. Kamae, J. Kataoka, S. Katsuda, J. Katsuta, M. Kawaharada, N. Kawai, T. Kawano, S. Kawasaki, D. Khangaluyan, C. Kilbourne, M. Kimball, M. Kimura, S. Kitamoto, T. Kitayama, T. Kohmura, M. Kokubun, S. Konami, T. Kosaka, A. Koujelev, K. Koyama, H. Krimm, A. Kubota, H. Kunieda, S. LaMassa, P. Laurent, F. Lebrun, M. Leutenegger, O. Limousin, M. Loewenstein, K. Long, D. Lumb, G. Madejski, Y. Maeda, K. Makishima, M. Markevitch, C. Masters, H. Matsumoto, K. Matsushita, D. McCammon, D. McGuinness, B. McNamara, J. Miko, J. Miller, E. Miller, S. Mineshige, K. Minesugi, I. Mitsuishi, T. Miyazawa, T. Mizuno, K. Mori, H. Mori, F. Moroso, T. Muench, K. Mukai, H. Murakami, T. Murakami, R. Mushotzky, H. Nagano, R. Nagino, T. Nakagawa, H. Nakajima, T. Nakamori, S. Nakashima, K. Nakazawa, Y. Namba, C. Natsukari, Y. Nishioka, M. Nobukawa, H. Noda, M. Nomachi, S. O'Dell, H. Odaka, H. Ogawa, M. Ogawa, K. Ogi, T. Ohashi, M. Ohno, M. Ohta, T.

#263186 http://dx.doi.org/10.1364/OE.24.025548
Journal © 2016 Received 25 Apr 2016; revised 21 Jul 2016; accepted 22 Aug 2016; published 24 Oct 2016

Optics EXPRESS

Okajima, T. Okazaki, N. Ota, M. Ozaki, F. Paerels, S. Paltani, A. Parmar, R. Petre, C. Pinto, M. Pohl, J. Pontius, F. S. Porter, K. Pottschmidt, B. Ramsey, R. Reis, C. Reynolds, C. Ricci, H. Russell, S. Safi-Harb, S. Saito, S.-i. Sakai, H. Sameshima, K. Sato, R. Sato, G. Sato, M. Sawada, P. Serlemitsos, H. Seta, Y. Shibano, M. Shida, T. Shimada, P. Shirron, A. Simionescu, C. Simmons, R. Smith, G. Sneiderman, Y. Soong, L. Stawarz, Y. Sugawara, S. Sugita, A. Szymkowiak, H. Tajima, H. Takahashi, H. Takahashi, S.-i. Takeda, Y. Takei, T. Tamagawa, K. Tamura, T. Tamura, T. Tanaka, Y. Tanaka, Y. Tanaka, M. Tashiro, Y. Tawara, Y. Terada, Y. Terashima, F. Tombesi, H. Tomida, Y. Tsuboi, M. Tsujimoto, H. Tsunemi, T. Tsuru, H. Uchida, H. Uchiyama, Y. Uchiyama, Y. Ueda, S. Ueda, S. Ueno, S. Uno, M. Urry, E. Ursino, C. de Vries, A. Wada, S. Watanabe, T. Watanabe, N. Werner, N. White, D. Wilkins, S. Yamada, T. Yamada, H. Yamaguchi, K. Yamaoka, N. Yamasaki, M. Yamauchi, S. Yamauchi, T. Yaqoob, Y. Yatsu, D. Yonetoku, A. Yoshida, T. Yuasa, I. Zhuravleva, A. Zoghbi, and J. ZuHone "The ASTRO-H X-ray astronomy satellite," Proc. SPIE **9144**, 914425 (2014).

2. Y. Soong, T. Okajima, P. J. Serlemitsos, S. L. Odell, B. D. Ramsey, M. V. Gubarev, M. Ishida, Y. Maeda, R. Iizuka, T. Hayashi, Y. Tawara, A. Furuzawa, H. Mori, T. Miyazawa, H. Kunieda, H. Awaki, S. Sugita, K. Tamura, K. Ishibashi, T. Izumiya, S. Minami, T. Sato, K. Tomikawa, N. Kikuchi, and T. Iwase "ASTRO-H Soft X-ray Telescope (SXT)," Proc. SPIE **9144**, 914428 (2014).
3. T. Kitayama, M. Bautz, M. Markevitch, K. Matsushita, S. Allen, M. Kawaharada, B. McNamara, N. Ota, H. Akamatsu, J. de Plaa, M. Galeazzi, G. Madejski, R. Main, E. Miller, K. Nakazawa, H. Russell, K. Sato, N. Sekiya, A. Simionescu, T. Tamura, Y. Uchida, E. Ursino, N. Werner, I. Zhuravleva, J. ZuHone, and ASTRO-H Science Working Group "ASTRO-H white paper - clusters of galaxies and related science," arXiv:1412.1176 (2014).
4. T. Tamura, R. Iizuka, Y. Maeda, K. Mitsuda, N. Y. Yamasaki, "An X-ray spectroscopic search for dark matter in the Perseus cluster with Suzaku," Pub. Astronomical Soc. Jpn. **67**, 23 (2015).
5. T. Sato, R. Iizuka, T. Hayashi, Y. Maeda, M. Ishida, K. Tomikawa, N. Kikuchi, T. Okajima, Y. Soong, P. Serlemitsos, H. Mori, T. Izumiya, and S. Minami, "Examining the angular resolution of the ASTRO-H Soft X-ray Telescopes," Journal of Astronomical Telescopes, Instruments, and Systems, accepted, (2016).
6. B. Aschenbach, H. Bräuninger, and G. Kettenring, "Design and construction of the ROSAT 5 arcsec mirror assembly," Adv. Space Res. **2(4)**, 251–254 (1982).
7. R. Petre, P. J. Serlemitsos, F. E. Marshall, K. Jahoda, H. Kunieda, "In-flight performance of the Broad-Band X-Ray Telescope," Multilayer Grazing Incidence X-Ray/EUV Opt. **1546**, 72–81 (1992).
8. P. J. Serlemitsos, L. Jalota, Y. Soong, H. Kunieda, Y. Tawara, Y. Tsusaka, H. Suzuki, Y. Sakima, T. Yamazaki, H. Yoshioka, A. Furuzawa, K. Yamashita, H. Awaki, M. Itoh, Y. Ogasaka, H. Honda, and Y. Uchibori, ""The X-ray telescope on board ASCA," Pub. Astronomical Soc. Jpn. **47**, 105–114 (1995).
9. G. Conti, E. Mattaini, E. Santambrogio, B. Sacco, G. Cusumano, O. Citterio, H. W. Braeuninger, and W. Burkert, "X-ray characteristics of the Italian X-Ray Astronomy Satellite (SAX) flight mirror units," Adv. Multilayer Grazing Incidence X-Ray/EUV/FUV Opt. **2279**, 101–109 (1994).
10. B. Aschenbach "Design, construction, and performance of the Rosat high-resolution X-ray mirror assembly," Appl. Opt. **27**, 1404–1413 (1988).
11. O. Citterio, P. Conconi, M. Ghigo, R. Loi, F. Mazzoleni, E. Poretti, G. Conti, T. Mineo, B. Sacco, H. W. Braeuninger, and W. Burkert "X-ray optics for the JET-X experiment aboard the Spectrum X satellite," Adv. Multilayer Grazing Incidence X-Ray/EUV/FUV Opt. **2279**, 480–492 (1994).
12. P. J. Serlemitsos, Serlemitsos, P. J., Y. Soong, K.-W. Chan, T. Okajima, J. P. Lehan, Y. Maeda, K. Itoh, H. Mori, R. Iizuka, A. Itoh, H. Inoue, S. Okada, Y. Yokoyama, Y. Itoh, M. Ebara, R. Nakamura, K. Suzuki, M. Ishida, A. Hayakawa, C. Inoue, S. Okuma, R. Kubota, M. Suzuki, T. Osawa, K. Yamashita, H. Kunieda, Y. Tawara, Y. Ogasaka, A. Furuzawa, K. Tamura, R. Shibata, Y. Haba, M. Naitou, and K. Misaki, "The X-Ray Telescope onboard Suzaku," Pub. Astronomical Soc. Jpn. **59**, 9–21 (2007).
13. A. Sagdeo, S. K. Rai, G. S. Lodha, K. P. Singh, N. Yadav, R. Dhawan, U. Tonpe, M. N. Vahia, "X-ray characterization of thin foil gold mirrors of a soft X-ray telescope for ASTROSAT. characterization of SXT mirrors by X-ray reflectivity," Experimental Astronomy **28**, 11–23 (2010).
14. B.L. Henke, E.M. Gullikson, and J.C. Davis. "X-ray interactions: photoabsorption, scattering, transmission, and reflection at E=50-30000 eV, Z=1- 92," Atomic Data Nucl. Data Tables **54 (2)**, 181–342 (1993).
15. M. A. Leutenegger, M. Audard, K. R. Boyce, G. V. Brown, M. P. Chiao, M. E. Eckart, R. Fujimoto, A. Furuzawa, M. Guainazzi, D. Haas, J. W. den Herder, T. Hayashi, R. Iizuka, M. Ishida, Y. Ishisaki, R. L. Kelley, N. Kikuchi, C. A. Kilbourne, S. Koyama, S. Kurashima, Y. Maeda, M. Markevitch, D. McCammon, K. Mitsuda, H. Mori, N. Nakaniwa, T. Okajima, S. Paltani, R. Petre, F. S. Porter, K. Sato, T. Sato, M. Sawada, P. J. Serlemitsos, H. Seta, G. Sneiderman, Y. Soong, S. Sugita, A. E. Szymkowiak, Y. Takei, M. Tashiro, Y. Tawara, M. Tsujimoto, C. P. de Vries, T. Watanabe, S. Yamada, and N. Yamasaki "In-flight verification of the calibration and performance of the ASTRO-H (Hitomi) Soft X-ray Spectrometer," Proc. SPIE **9905**, 106 (2016).
16. L. Nevot and P. Croce, "Caractérisation des surfaces par réflexion rasante de rayons X. Application à l'ètude du polissage de quelques verres silicates," Revue de Physique Appliquee, **15**(3), 761–779 (1980).
17. S. Kraft, J. Stümpel, P. Becker, and U. Kuetgens, "High resolution x-ray absorption spectroscopy with absolute energy calibration for the determination of absorption edge energies," Rev. Sci. Instrum. **67**, 681 (1996).
18. H. A. Kramers, "La diffusion de la lumiere par les atomes," Atti Cong. Intern. Fisici, (Transactions of Volta Centenary Congress) Como **2** 545–557 (1927).
19. R. de L. Kronig, "On the theory of the dispersion of X-rays," J. Opt. Soc. Am. **12**, 547–557 (1926).

Optics EXPRESS

1. Introduction

The international X-ray observatory ASTRO-H [1], later renamed HITOMI, was launched on February 17, 2016(JST). Two Soft X-ray Telescopes (SXT-I and SXT-S) are mounted on the ASTRO-H satellite [2]. The SXT-I and SXT-S focus X-ray images on the respective focal plane detectors of the CCD camera (SXI) and the micro-calorimeter (SXS).

The SXS boasts the unprecedentedly high energy resolution at the hard X-ray band (see below). One of the goals of the ASTRO-H mission is the first detection of a decay line from the hypothetical sterile neutrino in the keV mass range [3]. The sterile neutrino is one of the more likely candidates for the constituent of the dark matter, and if detected, it would be the first direct evidence of the mysterious dark-matter constituent. Many astronomers have searched for the line signal, yet to no avail, hampered presumably by both insufficient energy resolution of the past instruments and the instrumental edge structures (e.g., [4]), the latter of which smears out the weak line and pushes it below the detection limit. The ASTRO-H SXS has in principle a much higher potential to detect the line than any of the past X-ray instruments, due to its superior energy-resolution. However, very fine calibration of the effective area of the telescope SXT, particularly at around the gold edges, is essential to exploit fully the high resolution of the SXS.

The SXTs adopt the Wolter-I type optics with the reflector surface coated with gold. One of the hurdles in constructing the SXT response is to obtain the accurate reflectivity around the complex gold L edges, which appear in the 11–15 keV band. One of the issues of the SXTs response construction is then to know the reflectivity around the gold L edges that appears in the 11-15 keV band. In order to model the effective-area curve in the edge bands, the reflectivity of the SXT's gold surface with a precise energy pitch should be measured, on which we focus in this paper. Other issues are, and will be, separately addressed in our companion papers, such as [5].

In the past (and partly still active) X-ray missions of ROSAT [6], BBXRT [7], ASCA [8], BeppoSAX [9], XMM-Newton [10], Swift XRT [11], Suzaku [12], and ASTRO-SAT [13], a gold mono-layer was adopted for the reflector's surface in their optics. Since the energy resolution of their focal plane detectors is at best $E/\Delta E \sim 50$, reflectivity with a resolution better than 10 eV has not been required strongly. An existing cataloged table of the atomic scattering factor with a course energy pitch of 30 eV (e.g., [14]) should be suffice in modeling the effective area in the response function for the instruments onboard those satellites.

The energy resolution of the focal plane detector SXS-XCS of the ASTRO-H SXT-S is as good as ~5 eV at 6 keV [15], which corresponds to the resolution power of $\sim$ 1000. The reflectivity with an energy pitch with a few eV or better is required for the calculation of the effective area of the SXT.

Motivated with this, we have conducted the pre-flight experiment to measure the reflectivity of the reflectors of the ASTRO-H SXT for the energy range of 11–15 keV, using a synchrotron beamline at Spring-8. We here present the result of our experiment, in which we have accomplished the finest energy-pitch measurements of 0.4–0.7 eV, ever reported at this energy range for the SXT reflector.

2. Experiment

2.1. Reflectivity of a mono layer

The X-ray reflectivity of a mono layer is known to be dependent on the physical condition of the incident X-rays and the layers. The reflectivity is given by the following equation, using the Nevot-Croce exponential factor, which takes into account the effect of the surface roughness on X-ray scattering [16],

Optics EXPRESS

$$R = R_0 \exp\left(-n_i n_j \sin\theta_i \sin\theta_j \left(\frac{4\pi\sigma}{\lambda}\right)^2\right) \tag{1}$$

where R_0 is the ideal surface reflectivity calculated with the Fresnel equations, n_i and n_j are indices of refraction between the two layers, θ_i and θ_j are the incident and reflected angles of X-rays, and σ is the surface roughness. If the vacuum atmosphere for the incident space and specular reflection ($\theta_i = \theta_j = \theta$) are assumed, Eq. 1 is simplified as

$$R = R_0 \exp\left(-n \sin^2\theta \left(\frac{4\pi\sigma}{\lambda}\right)^2\right). \tag{2}$$

The complex refractive index of a layer consisting of a single element is

$$\tilde{n} = 1 - \delta - i\beta \tag{3}$$

where δ and β are related to the atomic scattering factors f1 and f2 via equations

$$\delta = \frac{N_a r_e}{2\pi}\lambda^2 f_1 \tag{4}$$

$$\beta = \frac{N_a r_e}{2\pi}\lambda^2 f_2 \tag{5}$$

and

$$N_a = (N_0/A)\rho \tag{6}$$

with the Avogadro constant N_0, a classical electron radius r_e, an atomic number A, a mass density ρ, and an X-ray wavelength λ.

The ideal surface reflectivity R_0 is then calculated as

$$R_0 = \frac{h - \frac{\theta}{\theta_c}\sqrt{2(h-1)}}{h + \frac{\theta}{\theta_c}\sqrt{2(h-1)}} \tag{7}$$

$$h = \left(\frac{\theta}{\theta_c}\right)^2 + \sqrt{\left(\left(\frac{\theta}{\theta_c}\right)^2 - 1\right)^2 + \left(\frac{\beta}{\delta}\right)^2} \tag{8}$$

where θ_c is a critical angle and is given by

$$\theta_c = \sqrt{2\delta}. \tag{9}$$

In summary, the reflectivity is a function of the energy (E or wavelength λ), incident angle (θ) of X-rays and roughness (σ), and mass density (ρ) and the atomic scattering factors ($f1$ and $f2$) of the surface layer. In order to obtain all these parameters for the ASTRO-H SXT reflector, we measure the reflectivity, using the witness sample.

2.2. Measurements

2.2.1. Spring-8 BL01B1

X-ray reflectivity was measured at the BL01-B1 beam line at the SPring-8 facility of the Japan Synchrotron Radiation Research Institute (Proposal numbers 2014A1471/2014B1475). Figure 1, which was originally published in the SPring-8 website

(http://www.spring8.or.jp/wkg/BL01B1/instrument/lang/INS-0000000401) illustrates a schematic arrangement of our setup of the beam shaping in the measurements.

The incident beam from the ring is reflected at two gracing angle mirrors and two crystals. From the ring side, the first collimating mirror, the first crystal, the second crystal and the second focusing mirror are positioned in this order. The two mirrors are positioned in front and rear of the two crystals.

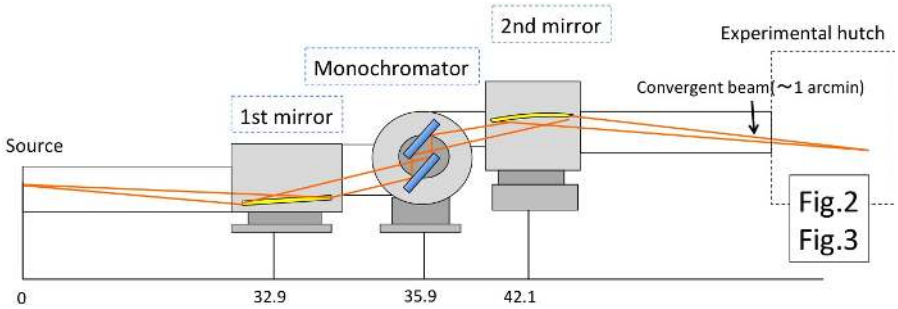

Fig. 1. Configuration for the monochromator system in our experiment at the Spring-8 BL01B1 beamline. The details of each component are listed in Table 1. The configuration around the sample at the experimental hutch is shown in Figs. 2 and 3.

Table 1. Mirrors and crystals in the beam line BL01B1

Mirrors.....		
	First collimating mirror	Second focusing mirror
Feature	Vertical collimation	Vertical focusing
	Higher harmonic elimination	Higher harmonic elimination
Size [mm]	$1000 \times 90 \times 50$	$1000 \times 90 \times 50$
Coating	Rh	Rh
Surface	Cylindrical bent	Cylindrical bent
Substrate	Si	SiO_2
Crystals.....		
	1st and 2nd crystals	
Diffraction plane	Si (311)	
Energy [keV]	7.1-72	
$\Delta E/E$	3×10^{-5}–2×10^{-4}	

For the material for the diffraction plane, Si(311) double-crystals (d = 1.63747Å) were chosen to cover the energy range of 9–16 keV. A typical photon flux at the position of a sample for a beam size of 10 mm (horizontal) × 0.2 mm (vertical) is 1×10^9–2×10^{10} photon s^{-1} in 7.1–72 keV.

The beamline scientists of BL01B1 had made careful tunings of the 1st mirror and the DCM. The shape of the 1st mirror was finely controlled and the purity of the energy was dominated by the rocking curve of the two crystals. The energy resolution was calibrated and was summarized as http://bl01b1.spring8.or.jp/technical/Resolution.gif.

The energy resolution of the beam is $\Delta E/E \sim 3\times10^{-5}$ (FWHM), which corresponds to 0.3 eV at ~ 10 keV. In contrast, the energy pitch of the DCM stage is 0.4 – 0.7 eV, which is the

Optics EXPRESS

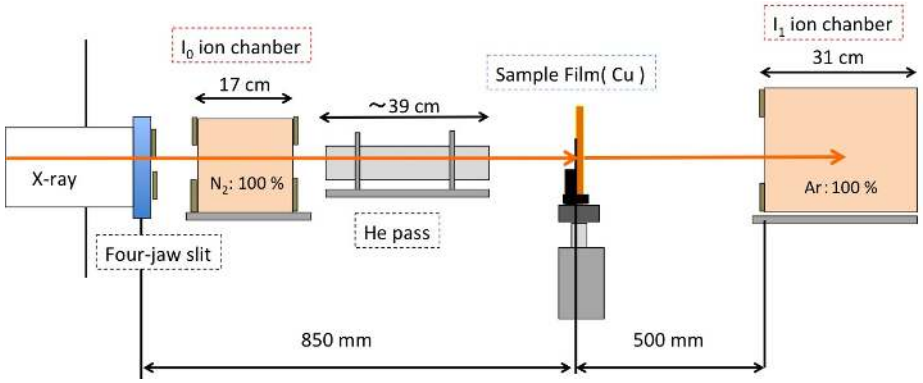

Fig. 2. Configuration at the experimental hutch for the energy calibration.

dominant factor that determines the energy resolution in our measurements.

The second mirror is designed to focus the beam to ~0.3 mm in height at the sample, which is located at 4.9 m away from the sample reflector. The mirrors are tilted to cut out high-energy photons; the tilt angle is tuned within the critical angle for the energy of ~20 keV (=3mrad). In the energy band of 9–16 keV, the higher harmonics are negligible. The diverging angle of the incident beam is limited with the viewing angle of the 1 m long second mirror viewed from the sample, which is about 0.04 degrees in full width. Since the 1 meter long mirror makes X-rays diverge to the vertical direction, the divergence is dominated to the vertical direction and is negligible to the horizontal direction.

The ion chambers are used to detect X-rays. Table 2 summarizes their dimensions. One chamber (I0) is mounted between the beam slit and the sample, whereas the other (I1) is mounted at the end. The output current of the ion chambers are read out with a current amplifier Keithley Current Amplifier 428. The output voltage is sent to the low-pass filter electronics and then is converted to a digital number with a combination of a voltage-frequency converter and a counter. Finally, we read the output counts of the ion chambers I0 and I1, and determine transmissivity of the foils and reflectivity of the reflectors.

2.2.2. Energy calibration

The calibration of the relation between the crystal angle and the energy was based on identification of the pre-edge of the Cu-K absorption at ~8.979 keV with the 1s− >3d(+4p) transition. The configuration for the transmission measurements is shown in Fig. 2. The 6μm-thick Cu film is used for the calibrator. Figure 4 plots the transmission spectra in units of the normalized transmissivity $\mu t = -log(I_1/I_0)$. Figure 4 also shows the first derivative of μt. We identified the local minimum of the derivatives as the Cu-K pre-edge. We then gave an offset of the crystal rotation stage to match the energy at the minimum as 8980.48 eV [17]. A typical error of the energy at the minimum is ~1 eV. To check our offset number, we measured the transmissivity of a 5μm-thick platinum foil. We found that the energy of the very sharp edge of the Pt-L2 transition was consistent with the cataloged value of 13.27190(3) keV within 1 eV [17]. We interpret this 1 eV error as the systematic uncertainty of the incident energy in our experiment in 11.2–15.4 keV. The offset is applied throughout our measurements.

Optics EXPRESS

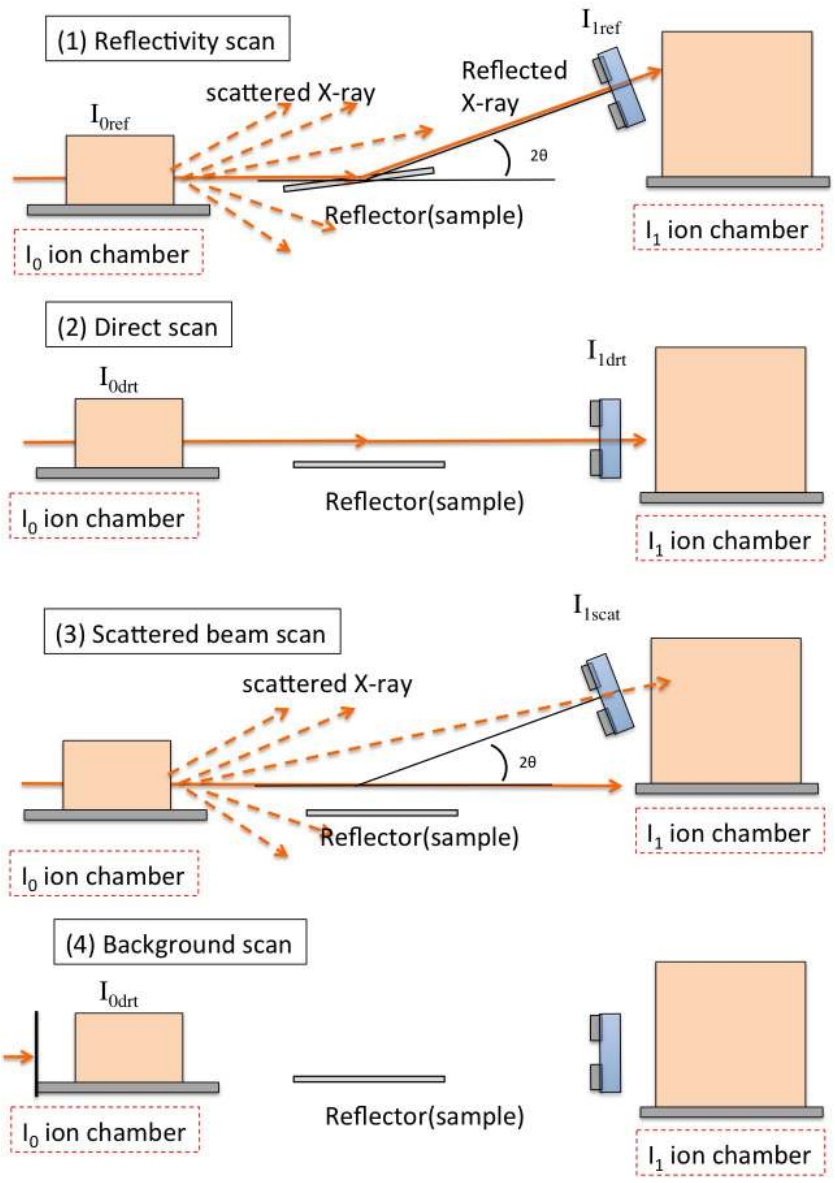

Fig. 3. Configuration at the experimental hutch for the reflectivity measurements. The four steps of (1) reflectivity, (2) direct, (3) scattering, and (4) background measurements are shown from top to bottom.

Optics EXPRESS

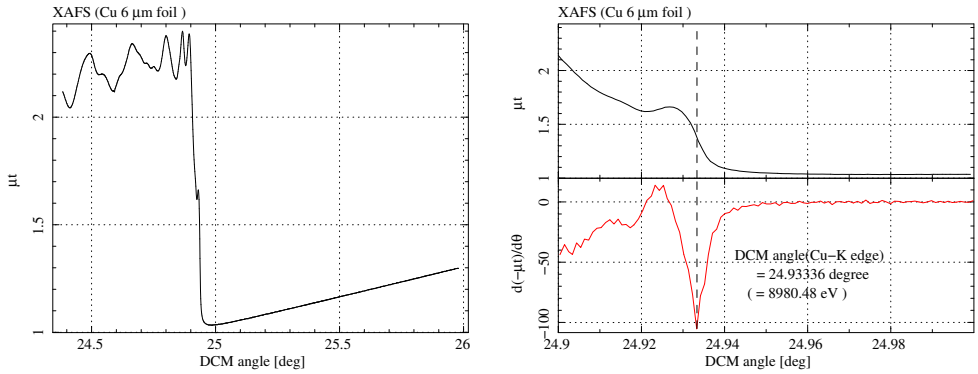

Fig. 4. Film transmissivity of the Cu 6μm-thick film. The normalized transmissivity in the 24.35–26.00 and 24.90–25.00 degrees are plotted in the left and right panels, respectively. The lower panel also shows its first derivative.

2.2.3. Sample stages and detectors

A schematic diagram for the reflectivity measurements is shown in Fig. 3. Our sample "reflector" [Fig. 5] is put on near the focus of the 2nd focusing mirror. In front and rear of the reflector, two ion chambers, designated respectively as I0 and I1, are placed. Four-jaw slits are installed in front of each ion chamber. The parameters for the ion chambers are summarized in Tables 2 and 3. A He pass tube with $\sim$ 40mm long is installed between I0 and the reflector in order to reduce the attenuation by air.

The reflector is put on a rotation θ-stage, whereas the four-jaw slit in front of I1 is on the 2θ-stage. The incident beam is shaped to 0.05 mm $\times$ 1 mm for the vertical (V) and horizontal (H) directions, respectively. The reflected beam passes through the 2nd four-jaw slit with 6 (V) mm $\times$ 1 (H) mm in front of the I1 detector. The position of the I1 detector is fixed. Regardless of the variable position of the slit on the 2θ-stage, it can accumulate the photons since the window vertical width is ~63 mm wide.

With the computer-controlled stages and detectors, the reflectivity is measured with the following four steps,

1. Measure the flux of the reflected beam ($I_{\mathrm{Ref}}(E,\theta)$), which includes the detector background and scattering at the air [Fig. 3(1)].
2. Remove sample and measure the flux of the direct beam ($I_{\mathrm{Drt}}(E,\theta)$), which includes the detector background and scattering at the air. The scattering should be negligible [Fig. 3(2)].
3. Move the detector to the position for reflection and measure the flux of the reflected beam. X-rays do not illuminate the reflector. The scatting at the air in the beam path is measured ($I_{\mathrm{Scat}}(E,\theta)$). The detector background is included [Fig. 3(3)].
4. Stop the beam and measure the detector background ($I_{\mathrm{Bkg}}(E,\theta)$) [Fig. 3(4)].

The reflectivity R is then calculated as

$$R = \left(\frac{I1_{\mathrm{Ref}} - I1_{\mathrm{Scat}}}{I0_{\mathrm{Ref}} - I0_{\mathrm{Scat}}}\right) / \left(\frac{I1_{\mathrm{Drt}} - I1_{\mathrm{Bkg}}}{I0_{\mathrm{Drt}} - I0_{\mathrm{Bkg}}}\right). \tag{10}$$

Optics EXPRESS

Two methods are conceivable for obtaining the reflectivity at a given energy E and at a given angle θ: angle scanning with the fixed energy (the angular scan) and energy scanning with the fixed angle (the energy scan). The angular scan is sensitive to all the surface parameters; thus we first performed an angular scan to determine the roughness and the mass density, as well as the atomic scattering factors. However, due to the limited machine time of the beamline, we could not measure the angular reflectivity with a fine energy-interval for the wide energy band of 11.2–15.2 keV. We then made an energy scan at ten incident angles and obtained the angular reflectivity at each angle. The configuration of the scans is summarized in Table 5

Table 2. The ionization chamber (Ohyo Koken Kogyo Co., Ltd)

Model	Electrode Length (mm)	Chamber Length (mm)	Distance Between Electrodes (mm)	Window Height × Width (mm)	Approximate Weight (kg)
S-1194B1	140	170	12.5	10× ~ 63	2.4
S-1196B1	280	310	12.5	10× ~ 63	3.8

http://www.oken.co.jp/web_oken/Ics_i1_en.htm.
Incident window material is 50μm thick polyimide.

Table 3. Ion-chamber gas parameters

Ion chamber	I0	I1
Used model	S-1194B1	S-1196B1
Gas material	Ar 15%/N_2 85%	Ar 100%
Attenuation at 760 (Torr)		
at 11.2 (keV)	22.3%	91.8%
at 14.0 (keV)	12.4%	73.0%
at 15.4 (keV)	9.54%	62.9%

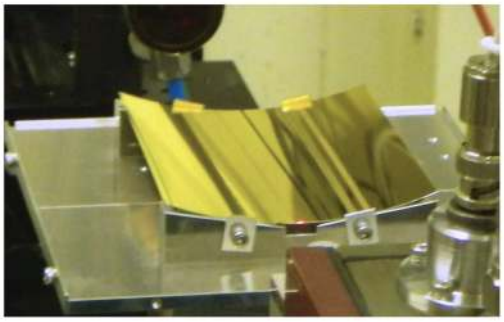

Fig. 5. Photo of our witness sample. Details are summarized in Table 4.

Optics EXPRESS

Table 4. Sample Reflector

Type		Replica Foil
Layers		Gold ~2000[Å] / Epoxy 10μm / Aluminum 152 μm
Size	Height	101.6 [mm]
	Width	88 [mm]
	Radius	114 [mm]

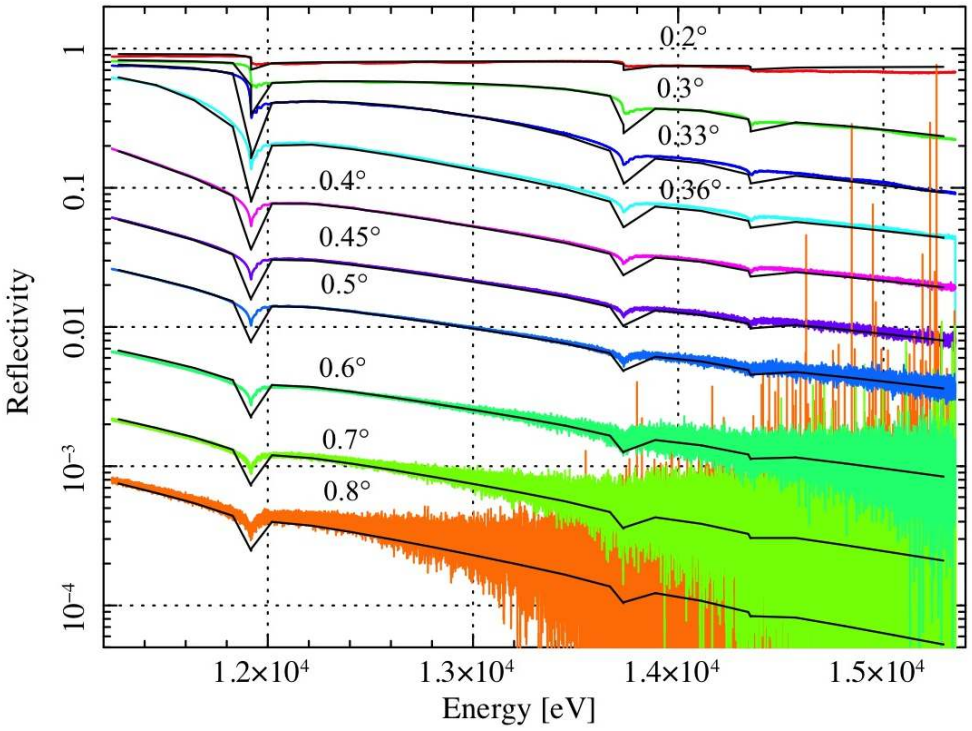

Fig. 6. Reflectivity taken with the energy scan. The colored data-points are our measurements, whereas the black data-points are calculated, using the HENKE table. The errors are in 1-σ confidence.

3. Analysis and results

The reflectivity is obtained with Eq. 10. Figure 6 plots the reflectivity obtained with the energy-scan. We obtained energy-pitch measurements of 0.4–0.7 eV for the SXT reflector, the finest ever reported in the 11.2 – 15.2 keV range were obtained. The edges associated with the L-I, II, and III transitions are identified, of which the depths are found to be roughly 60% shallower than those expected from Henke's atomic scattering factors.

Figure 7 plots the angular reflectivities obtained with the angular-scan and energy-scan. The angular reflectivity obtained with the angular-scan is then fitted with the Nevot-Croce model [Eq. 2]. The free parameters are the roughness σ, the atomic scattering factors f1 and f2, an offset of the incident angles θ, and a shift of the beam position. The latter two originate from the beam wobbling mentioned below.

Optics EXPRESS

Table 5. Data taken for the SXT reflector

Angular scan	Band degree	Pitch degree	Energy keV
	0.00-1.00	0.01	11.200, 12.000, 13.000, 14.000, 14.500, 15.400

Energy scan	Band keV	Pitch eV	Incident angle degree
	11.24–15.35	0.4–0.7	0.20,0.30,0.33,0.36,0.40,0.45,0.50,0.60,0.70,0.80

Table 6. Energy and angles used for the curve fitting

Energy keV	Fit Range degree
Angular Scan	
11.200	0.30–0.50
12.000	0.30–0.45
13.000	0.25–0.60
14.000	0.20–0.42
14.500	0.20–0.40
15.400	0.20–0.45
Energy Scan	
11.240–14.000	0.30–0.60
14.000–15.350	0.20–0.60

Spring-8 BL01 that we used is originally designed to measure the X-ray Absorption Fine Structure (XAFS) with the transmission method. The beam height and angle at the sample position are slightly wobbled within the field of view of the secondary mirror from the slit. The wobbling is not under control. Therefore the resultant uncertainties in the beam position and angle are up to 0.3 mm and 0.04 degrees, respectively. A slight change in the beam angle (i.e., tilt) and/or position (i.e., shift) from the optimum leads to an offset to the incident angle and/or a change in the flux of the reflection at a small incident angle below ~0.2 degrees, respectively.

In the fitting, we found that the offset incident-angle is energy dependent and fluctuated up to ~0.6 arcmin. The best-fit value of the shift also varies from scan to scan within 0.14 mm. The shift causes the reflectivity below 0.2 degrees to vary significantly from scan to scan. Since the cause of this shift is not under control, we screen the data at low incident-angle for the model fitting . Furthermore, some data at the large off-axis angle are not modeled well [Fig. 7]. The cause is presumably due to the low signal-to-noise ratio, but it is not understood well. We also removed the data at large off-axis angles. The regions of interest of the data after the screenings are applied are summarized in Table 6. After applying the correction and screening above, the reflectivity of the angular scan was refitted and was found to be well reproduced with the combination of the roughness σ = 8.4Å and the mass density ρ = 19.32 g/cc (bulk density for gold) as well as the atomic scattering factors f1 and f2. The best-fit factors are plotted in 8.

In Fig. 7, we also plotted the angular reflectivity using the energy scan data. We modeled the offset angle for the angular scan data as a function of energy and applied it for the analysis of the energy-scan data. The large detector noise is clearly visible in the energy scan plot [Fig. 6].

Optics EXPRESS

We calculate the standard deviation of the flux, choosing the data in their nearby featureless band, and estimate the noise, displayed as errors in Fig. 6. The reflectivity taken at the large incident angles of 0.6–0.8 degrees are mostly scattered, because the reflectivity at large incident angles is not high, and because the data are dominated with the detector noise. Hence, the noisy data at a large off-axis angle are also screened out. The regions of interest of the data after the screenings are applied are summarized in Table 6. Since the number of the angular data-points is limited, we fixed the roughness and mass density to be those obtained with the angular scan data and fit them with the two free parameters f1 and f2. The best-fit atomic scattering factors are shown in Fig. 8 and in Data File 1. Their errors are also listed as Δf_1 and Δf_2 in Data File 1.

We determined the atomic scattering factors f1 and f2, fitting the angular curve to the screened reflectivity. Figure 8 plots the results with red dots with the error bars 90 % confidence level. Our measurement is in good agreement with the HENKE table [14] in the energy band between 12.2

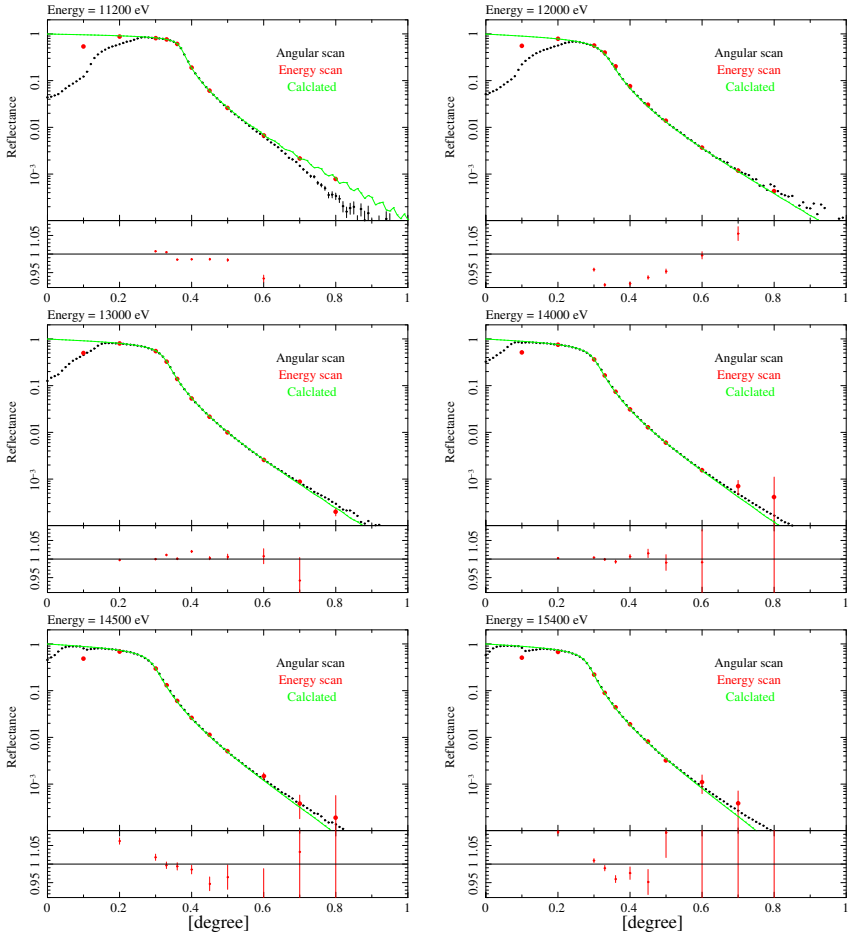

Fig. 7. Reflectivity taken with the angular (black dot) and energy scans (red dot). The green line corresponds to the best-fit model for the angular scan. In the lower panel in each figure, the red dots correspond to the ratio of the best-fit model for the angular scan to the energy scan data. From top left to bottom right, the beam energies are 11.2, 12.0, 13.0, 14.0, 14.5, 15.4 keV.

and 13.4 keV. However, it shows a prominent discrepancy at the edge energies (L_I at 14.3528 keV, L_{II} at 13.7336 keV, L_{III} at 11.9187 keV), which is probably due to the energy pitch in our measurements being finer than that in the Henke table. In the f2 factor, the fine structure around the gold L_{III} edge is visible at 12 keV [Fig. 8]. It is identified as the XAFS structures of gold. Similar discrepancies can be spotted at the deepest structures in the other edges of L_{II} and L_I, but are marginal due to the large errors. Our measured f2 factors are found to be overall consistent with those in the Henke table within the margin of error except near the XAFS structures at L_{III} edges. We should note that the f2 factor at the energy above 14 keV is poorly constrained due to a larger error.

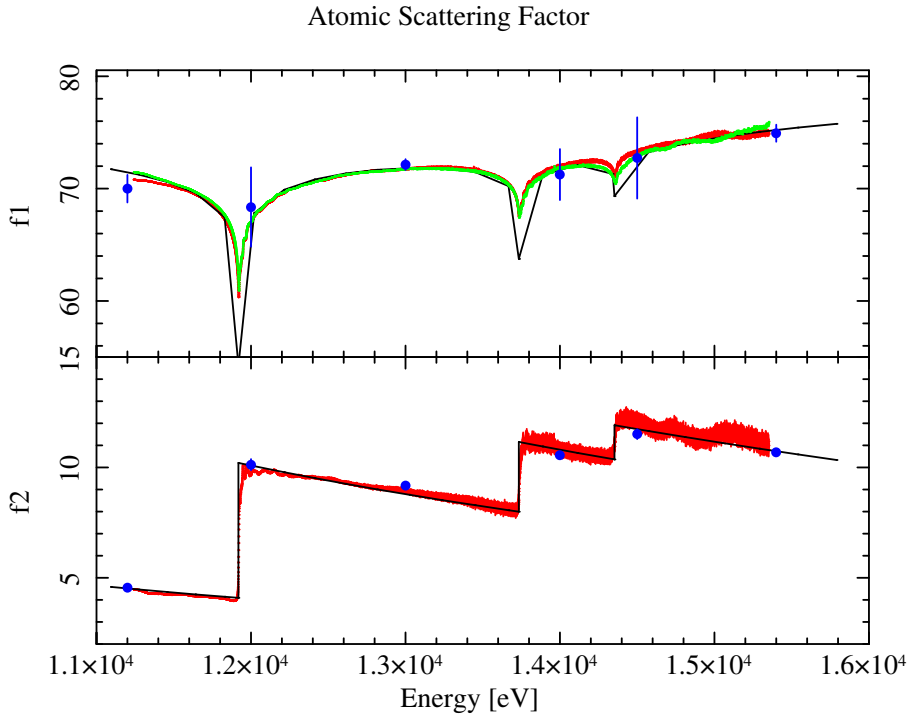

Fig. 8. Atomic scattering factors f1 (upper panel) and f2 (lower panel). The blue and red points show the factors obtained by the curve-fitting for the angular and energy scans, respectively. The green points (designated as f1′ in text) are calculated from the f2 factor, using the Kramers-Kronig relations. The error bars are in 90% confidence.

Since the f2 factors are consistent with the cataloged values by HENKE [14], we calculate the f1 factors from f2, using the Kramers-Kronig relations [18, 19]. The Kramers-Kronig relations are bidirectional mathematical relations, connecting the real and imaginary parts of any complex function that is analytic in the upper half-plane. These relations are applied to calculate analytically the real part f1 from the imaginary part f2 of the atomic scattering factor:

$$f_1(E) = Z + \frac{1}{\pi r_e hc}\int_0^\infty \mu(\epsilon)\frac{\epsilon^2}{E^2-\epsilon^2}d\epsilon - \Delta_{\text{rel}} \tag{11}$$

$$f_2(E) = \frac{1}{2\pi r_e hc} E\mu(E) \tag{12}$$

where Z is an atomic number, h is the Planck constant, c is the speed of light, and Δ_{rel} is the

relativistic correction factor $(Z/82.5)^{2.37}$ for gold. We used the f2 factors in the 11.2–15.2 keV range and the HENKE factors in the other energies. Substituting the f2 factors into the equations, we calculate the f1 factors (hereafter designated as f1′), and plotted them in Fig. 8 upper panel with green points. The difference between the two solutions f1 and f1′ are listed as $\Delta f_1'$ in Data File 1.

One may wonder why the edge is so deep for the f1 or the reflectivity for the HENKE table. We consider it to be primarily due to the unequal and simplified spacing in energy in the HENKE table. They first measured the f2 parameter and then calculated the f1 parameter, using the KK relations. In Eq. 12, the term of $\epsilon^2/(E^2-\epsilon^2)$ becomes large if $E-\epsilon$ is small. Therefore, the f2 parameter at the nearest energy $\epsilon_{\rm nearest}$ to the energy E mostly contributes to the f1 parameter.

In the HENKE table, the shape of the f2 edge is described only by two surrounding energies, for example, L_{II} edge is by 13.7335 and 13.7337 keV, and the separation between the two energies can be as small as 0.2 eV. The fine and simple energy spacing of an edge makes a sharper edge in the f2 parameter than the true value. The sharper edge in f2 makes a deep dip in the f1 parameter. For that reason, we believe that the HENKE values of f2 are accurate. However, the energy intervals are too simple in the table – very fine and simple at the edge energy but coarse elsewhere. The fine and simple energy pitch at the edge makes an unrealistically deep dip at the edge with the f1 parameter in their table.

4. Discussion

4.1. Uncertainty of the atomic scattering factor and the calculated reflectivity

We examine our two solutions of the factor f1 (red and green points in the upper panel of Fig. 8). If the factor f1 was perfectly determined, the two solutions f1 and f1′ should agree with each other. In our case, they didn't exactly, and the difference is much larger than their statistical errors. We interpret the difference between f1 and f1′, which originated from the uncontrolled beam tilt and shift of the incident beam (Section 3.1), as a systematic error in our estimate, and present the result in this section.

Our primary motivation is to apply the factor to the response function of the ASTRO-H SXT. We thus investigate the effect of the f1 and f2 errors to the reflectivity.

First, we calculate the reflectivity at the incident angles of 0.15, 0.30, 0.45 and 0.60 degrees, substituting the f1 and f2 factors into Eq. 2. The top panel of Fig. 9 shows the obtained reflectivities, where the errors of the f1 and f2 factors are propagated. Also, we calculate the reflectivity, based on the combination of the f1′ and f2 factors. We then calculate the ratio of the former to the latter, and plotted in the lower four panels in Fig. 9, putting the same error point to both the positive and negative sides of each data point. The ratio can be regarded as a systematic uncertainty in our measurement of the reflectivity, calculated from the atomic scattering factors that we have derived.

Notably, the errors at small incident angles are fairly small, presumably because the reflectivity is very close to unity and therefore is not sensitive to the errors of the factors f1 and f2. At larger incident angles of 0.30, 0.45 and 0.60 degrees, the error is large, particularly for the highest-energy band of 14–15 keV. The critical angle drops as the energy increases and is smaller than 0.3 degrees at these high energies; accordingly, the reflectivity also sharply drops. Consequently, the reflectivity is expected to be, and is, very sensitive to the error of the f1 and f2 factors at high-energy bands [Fig. 9].

4.2. Uncertainty of the SXT effective area

The SXTs are thin-foil-nested Wolter-I X-ray telescopes [2]. The angles of primary reflectors in the SXTs are designed to follow a function of the radius between roughly 0.15–0.58 degrees for the innermost to outermost reflectors. More inside a reflector is, smaller the angle is, and

Optics EXPRESS

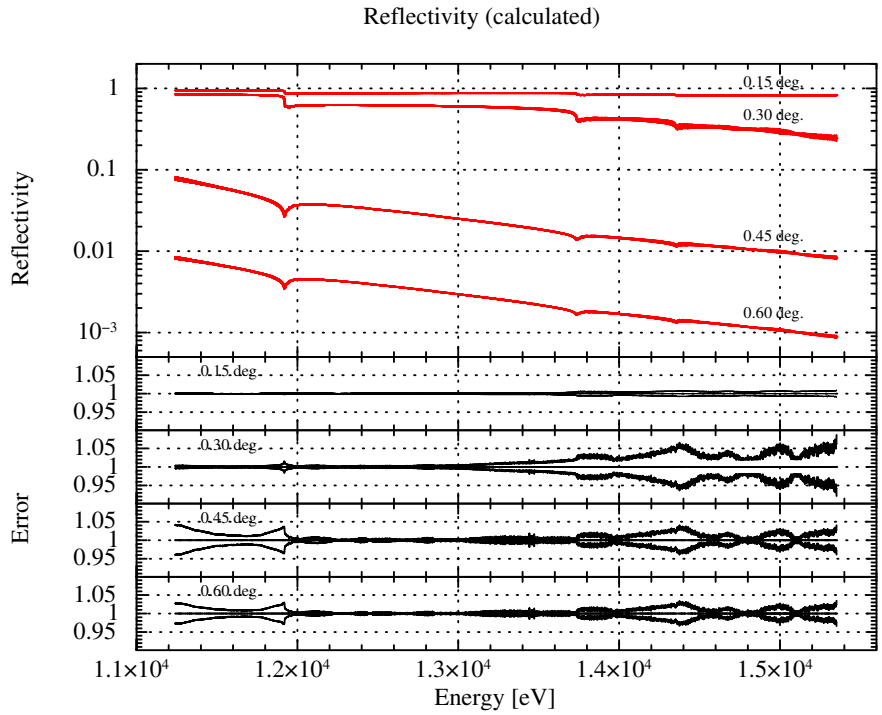

Fig. 9. Reflectivity calculated from the measured f1 and f2 factors at 0.15, 0.30, 0.45 and 0.60 degrees (top panel). The error bars are in 90% confidence level. The bottom four panels show the "error" ratio between the reflectivities for four different angles (see text).

therefore more efficiently it reflects incoming X-rays.

The SXT adopts a conical approximation [2]. Assuming the light from the direction of the optical axis, the reflected light at the primary mirror is reflected at the same angle at the secondary reflector. It means that each reflector pairs at a given radius shell has the unique incident angle. So, we can simply calculate the effective area by multiplying the geometrical area by the square of the reflectivity for the angle. We repeated this calculation for all the reflectivity pairs. Note that any figure errors of the reflectors, which can change the incident angle, are ignored in this calculation.

The geometry in the reflector configurations is the primary factor to determine the effective area. The height of the reflector is the same at any radius in the SXTs, whereas the angle of tilt is proportional to the radius. Then the effective area of a reflector is proportional to the square of the radius, since the circumference is proportional to the radius. We calculate the effective area of the telescope by multiplying the reflector's effective area at each radius by its reflectivity, and plot it in Fig. 10. Note that the reflectivity is multiplied by twice in the calculation, because each set of the reflectors consists of two parts, the primary and secondary ones.

The reflectivity R drops exponentially at around $R \sim 1/e$ (~0.37), at which the grazing-angle of the point is called the critical angle. The reflectivity for the incident grazing-angles smaller than the critical angle is, on the other hand, all close to unity. Hence, the systematic error of the reflectivity is expected to be in general small, and so indeed is as derived in our experiments, particularly at the energy below 13.6 keV of the Au L_{II}-edge [Fig. 9]. Thus, the error of the effective area of the SXT is calculated to be also small, roughly 2% at the energy below 13.6 keV.

Optics EXPRESS

However, a distinctive trend of increase in the error is observed at the energy above 13.6 keV, up to ~4% for the resultant effective area. The cause of this trend is explained as follows. Higher the energy of incident X-rays is, higher the critical angle of reflection is, and less reflectors in the telescope have the angle smaller than the critical angle (hereafter we refer to them as "sub-critical" reflectors); as a result, most of reflectors except for the innermost reflectors have the angle larger than the critical angle for the highest-energy X-rays (referred to as "above-critical" reflectors). Then, the total contribution from the "above-critical" reflectors is, though the reflectivity of each of those is smaller than that of the "sub-critical" reflectors, significant for high-energy X-rays. The systematic error of the reflectivity of the "above-critical" reflectors is larger than that of the "sub-critical" reflectors. Consequently, the systematic errors of the reflectivity, and hence of the calculated effective area, are considerably larger in the higher energy.

Another trend observed is marginally larger errors than the nominal 2% below the energy of 12 keV [Fig. 9]. It seems to be attributed to some settings in our experiments. However, the quantitative evaluation is difficult, and the cause is not fully understood.

We conclude that the systematic error originated from the uncertainty of the atomic scattering factors is up to about 4% for the SXT effective area in the energy range of 11.2–15.4 keV, for which we studied.

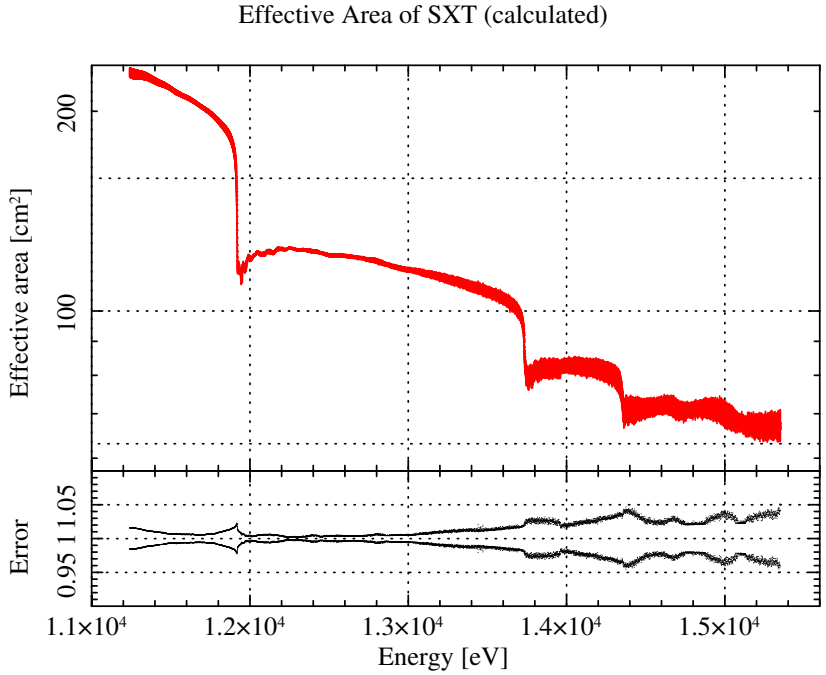

Fig. 10. Effective area of an ASTRO-H SXT (upper panel) with the error ratio (lower panel). The effective area is calculated, based on the design parameter [2] and the measured f1 and f2 factors of reflectivity of the reflectors. The errors are propagated from those of the f1 and f2 factors.

5. Conclusion

1. The reflectivity of the SXT's reflectors, which consist of a gold mono-layer, was measured for the energy range of 11.2–15.4 keV with the energy pitch of 0.4–0.7 eV.

Optics EXPRESS

2. We found that the uncertainty of the reflectivity is dominated by (1) the uncontrolled beam tilt and shift and (2) the detector noise due to the limited beam intensity.

3. The atomic scattering-factors f1 and f2 were determined with the unprecedented accuracy, where the reflectivity data that have a large uncertainty are screened out. Two solutions of the f1 and f2 factors are presented; one was determined with the curve fitting, and the other, calculated with the KK relations. The best-fit roughness on the surface was ~ 8.4Å in the NC curve fitting.

4. The reflectivity of the reflector and the effective area of the SXT were calculated, based on the f1 and f2 factors. The uncertainty of the measured effective area is likely to be at most 4% or even smaller.

Acknowledgments

The authors are grateful to all the full-time engineers and part-time workers in the GSFC/NASA laboratory for support in mass production of the Soft X-ray Telescope reflectors. R.I. and Y.M. acknowledge Support from the Grants-in-Aid for Scientific Research (numbers 25870744, 25105516 and 23540280) by the Ministry of Education, Culture, Sports, Science and Technology, Japan. We thank M. Sakano (Wise Babel Ltd.) and Chris Baluta for English correction.